# Low Bias Electron Scattering in Structure-Identified Single Wall Carbon Nanotubes: Role of Substrate Polar Phonons

Bhupesh Chandra, Vasili Perebeinos, Stéphane Berciaud, Jyoti Katoch, Masa Ishigami, Philip Kim, Tony F. Heinz, and James Hone

Phys. Rev. Lett. **107**, 146601 — Published 28 September 2011

DOI: 10.1103/PhysRevLett.107.146601

# Low bias electron scattering in structure-identified single wall carbon nanotubes: Role of substrate polar phonons

Bhupesh Chandra*[#†], Vasilli Perebeinos[#], Stéphane Berciaud[§¶], Jyoti Katoch[‡], Masa Ishigami[‡], Philip Kim[§], Tony F. Heinz[§], James Hone[†]

[†]Department of Mechanical Engineering, Columbia University, New York, NY10027

[#]IBM Research Division, T.J. Watson Research Center, Yorktown Heights, NY10598

[§]Department of Physics, Columbia University, New York, NY 10027

[‡]Department of Physics and Nanoscience Technology Center, University of Central Florida, Orlando, FL 32816

[¶]IPCMS (UMR 7504), CNRS and Université de Strasbourg, F-67034 Strasbourg, France

* To whom correspondence should be addressed. E-mail: bchandr@us.ibm.com, Tel: 914-945-2999, Fax: 914-945-4257

**Abstract**

We have performed temperature dependent electrical transport measurements on known structure single wall carbon nanotubes at low bias. The experiments show a superlinear increase in nanotube resistivity with temperature, which is in contradiction with the linear dependence expected from nanotube acoustic-phonon scattering. The measured electron mean free path is also much lower than expected, especially at medium to high temperatures (>100K). A theoretical model that includes scattering due to surface polar phonon (SPP) modes of the substrates reproduces the experiments very well. The role of surface phonons is further confirmed by resistivity measurements of nanotubes on aluminum nitride.

Discovered nearly two decades ago, single wall carbon nanotubes (SWNTs) remain one of the most promising candidates for applications in nanoscale electronic circuits elements such as field effect transistors and on-chip interconnects [1-2]. However, in spite of many years of study, the factors that determine the temperature-dependent electronic mean free path $L_m$ are still not well understood from an experimental standpoint [3-6]. At low temperatures and small bias voltages, defect- free carbon nanotubes are reported to display $L_m$ close to 8 μm [4], while at higher temperatures, $L_m$ decreases, with measured room-temperature values in the range of 0.2-1.2 μm [4-5, 9]. Except for results from ref. 5, all reported room-temperature values are ~ 2 to 3 times lower than the predicted $L_m$ due to intrinsic phonon scattering [8, 10-11].

A significant obstacle to better understanding of electronic transport in nanotubes has been incomplete structural information about the nanotube under study. Measurements of $L_m$ to date have relied upon techniques such as atomic force microscopy (AFM) and high-field current saturation[12] to determine nanotube diameter and ascertain whether a single tube or a small bundle of tubes is being studied. However, these techniques have a significant margin of error, and cannot give the (n,m) chiral indices, making precise comparison with theory difficult.

Here we report temperature-dependent resistivity measurements of chirally determined SWNTs, over a wide temperature range, and (for one sample) in ultrahigh vacuum. The experimental findings, supported by theoretical calculations, reveal the dominant role of surface polar phonons (SPP) of the underlying substrates in scattering nanotube carriers. The presence of extra scattering due to SPP modes, in addition to nanotube phonons, conclusively explains the low room-temperature $L_m$ values obtained in experiments so far.

Sample fabrication begins with deposition of Fe/Mo catalyst on Si substrates with narrow slits etched completely though the wafer. SWNTs are grown by chemical vapor deposition

(CVD) with ethanol as a feedstock, to yield freely-suspended nanotubes across the slit [13-14]. The nanotubes are then characterized by Rayleigh scattering spectroscopy [15-16] for structure assignment. For electronic measurements, structure-identified SWNTs are transfer-printed onto degenerately doped Si wafers with 300 nm $SiO_2$ epilayers [17]. Atomic force microscopy (AFM) is then used to determine the position of transferred SWNT relative to pre-patterned metal alignment marks. Figure 1a shows the AFM image of a transferred (26,11) metallic SWNT. Electron beam lithography is used to pattern palladium contacts of width 800 nm over the SWNT with varying channel lengths (0.2 μm -20 μm, given by the distance between contact edges), as shown in figure 1b.

The conductance of the SWNT devices is measured in a three-terminal configuration, with the Si wafer as the back gate, using low-frequency lock-in detection to minimize noise. Figure 2a shows device conductance G vs. back gate voltage ($V_g$) for the (26,11) metallic SWNT for different tube length segments. The (26,11) SWNT possess a small band gap due to curvature and electron-electron interactions [18-19], which can be seen as a dip in the conductance. Away from the band gap region, the current becomes independent of $V_g$; we use the p-channel branch (negative $V_g$), which has higher conductance than n-channel due to a lower Schottky barrier [20], to obtain the resistance. In the diffusive regime, the device resistance is $R = \rho L + \frac{h}{4e^2} + R_C$, where ρ is the nanotube resistivity, L is the channel length, $\frac{h}{4e^2} \approx 6.5k\Omega$ is the quantized conductance of a (4-fold degenerate) ballistic 1D channel, and $R_C$ is the extra resistance due to imperfect contacts. To extract ρ, R is plotted as a function of L, as shown in figure 2b; for this device, the slope gives ρ = 9.4 kΩ/μm at room temperature. The mean free path is given by $L_m = 6.5k\Omega/\rho$, and is ~0.7 μm at room T, on par with the best room temperature values

published so far [4, 9]. For $L<<L_m$, the SWNT channel becomes ballistic and R ~ 6.5 kΩ + $R_C$ (figure 2b). The measured value of $R_C$ is 2.5 kΩ for this device, indicating that the contacts are highly transparent outside the band-gap region. Figures 2c and 2d show the temperature dependence of the device properties. As expected, both the resistance (Fig. 2c) and resistivity (slope of lines in Fig. 2d) decrease with decreasing temperature.

In order to provide the best possible dataset with which to compare theory to experiment, the devices were measured over a wide temperature range (up to 475 K) in ultrahigh vacuum (UHV) conditions ($5 \times 10^{-10}$ Torr), to rule out contributions from adsorbate-induced resistivity. Figure 3 shows the temperature-dependent resistivity of the (26,11) nanotube, where ρ was extracted by fitting R vs. L as above. The resistivity increases with temperature in a super-linear fashion, reaching a value of 25 kΩ/μm at 475 K.

Models of electron-phonon scattering in nanotubes predict a roughly linear temperature dependence of the resistivity, which seems to be in conflict with the measured data. For instance, the dot-dashed line in Fig. 3 shows the resistivity calculated using a simple model $\rho(T) = \rho_{static} + \rho_{e-p}(T)$. Here $\rho_{static}$ is a free parameter representing the temperature-independent resistivity due to defects and fixed scattering sites, and has a value of 1.8 kΩ/μm for this nanotube. The linear slope of the resistivity due to electron-phonon scattering, $\rho_{e-p}(T)$, is given by the model for acoustic phonon scattering in [5]. Clearly, the acoustic-phonon carrier scattering model alone is unable to explain the observed results, particularly the super-linear temperature dependence of ρ. It also greatly underestimates the magnitude of ρ, by a factor of ~4 at high temperature.

In order to examine whether the observed super-linear temperature dependence of ρ could arise from SWNT optical phonon modes[21], a numerical model is developed that

calculates ρ(T) by solving Boltzmann transport equation using a single electron-phonon coupling g=5.3 eV/Å [10]. This value of g provides the strength of the scattering matrix element with all the vibrational modes in the CNT structure described by the phonon model [22]. The solid blue line in figure 3 represents the results from this model for the measured (26,11) SWNT. This model does indeed cause non-linearity in ρ(T). However, the calculated magnitude of the additional scattering is not sufficient to explain the experiments. More fundamentally, the onset of optical phonon scattering (~300K) reflects the frequency of the radial breathing mode (RBM), which has a well-established dependence on nanotube structure. Therefore, use of a structurally defined nanotube allows us to definitively rule out RBM scattering as the source of the observed super-linear ρ(T) behavior from 100-300 K.

Ruling out contributions from acoustic and optical nanotube phonons as well as adsorbate induced scattering leaves only phonon modes of the underlying substrates as the cause for reducing the electronic mean free path of nanotubes. Similar substrate phonons have been shown to play a large role in transport properties of graphene [23] and a theoretical study on semiconducting SWNTs predicted the surface polar phonons (SPP) modes to be important [24]. To investigate the role of SPP scattering on metallic SWNT transport, its effect is included in the resistivity calculations for the (26, 11) SWNT. The strength of the SPP phonon scattering depends on the distance from CNT to the polar substrate *h* and the dielectric properties of the substrate [25]. The coupling is strongest when the azimuthal angular momentum is conserved [26], for which case scattering rate of an electron with momentum *k* has a form [24]:

$$\frac{1}{\tau_k} = \frac{2\pi}{\hbar}\int dq \frac{e^2 \hbar\omega_{so}}{\pi}\left(\frac{1}{\kappa_\infty + 1} - \frac{1}{\kappa_0 + 1}\right)\frac{e^{-2hq}}{qd\sqrt{2\pi q\left(d+2h\right)}} \times \left[n_{so}\delta\left(\varepsilon_k - \varepsilon_{k+q} + \hbar\omega_{so}\right) + \left(1+n_{so}\right)\delta\left(\varepsilon_k - \varepsilon_{k+q} - \hbar\omega_{so}\right)\right] \quad (1)$$

where and $\kappa_0$ and $\kappa_\infty$ are the low- and high-frequency dielectric constants of the polar substrate, *d* is tube diameter, $\hbar\omega_{so}$ is the SPP energy and $n_{so}$ is the Bose-Einstein occupation number, which leads to the activated temperature dependence. These material properties can be measured independently and we use their values for $SiO_2$ [26] and AlN [27]. The distance from the CNT to the substrate is fixed at the van der Waals distance of h=3.5 Å. The temperature dependence shown in Fig. 3 is measured when device is in the on-state, i.e. $V_g$-$V_n$=8 V, where $V_n$ is a gate voltage corresponding to the CNT in the charge neutral state. Using a classical electrostatic capacitance $C_g=2\pi\varepsilon\varepsilon_0/\ln(4t/d)\approx0.34$ pF/cm for CNT on t=300 nm $SiO_2$ with ε=3.9, we can estimate a charge carrier density of n ≈ 1.7 e/nm. For such charge carrier density, the Fermi level is expected to lie within the first metallic band in a ~2 nm diameter CNT. Figure 3 shows the simulated temperature-dependent resistivity including SPP scattering for this doping level (solid red line). The SPP model accurately predicts the superlinear trend as well as absolute resistivity values. The robustness of the fit, particularly its dependence on the distance to the substrate *h*, is discussed in detail in the supporting information. When *h* is changed by ±30%, there is a 15-20% change observed in ρ(400K). Most importantly, because the onset temperature of SPP scattering depends on only on the known SPP energy, the close agreement between theory and experiment for the onset of super-linear behavior in $\rho(T)$ at ~100K provides direct evidence for the SPP scattering mechanism that does not depend on any adjustable parameters.

This significant effect of SPP scattering in SWNTs suggests that dielectric materials with higher SPP frequencies should increase the room-temperature mean free path. To observe the effect of changing substrate material on SPP scattering, a ~2 nm diameter semiconducting SWNT (with undetermined chirality) is transfer printed on an AlN layer deposited over degenerately doped silicon. Figure 4 compares the temperature dependence of $L_m$ for the previously-described

(26,11) SWNT on $SiO_2$, and the semiconducting SWNT on AlN. The fitted lines represent the numerical model results with and without the inclusion of SPP scattering from respective substrates. The numerical model accurately predicts the experiments on the AlN surface (at $n$ = *1.1*e/nm). The vertical dotted lines point to the onset temperature of the SPP scattering modes. It is clear from figure 4 that AlN surface phonon modes start contributing to carrier scattering at a much higher temperature than on $SiO_2$. This provides further confirmation of the SPP scattering model, and also indicates that substrate materials with higher SPP energies such as AlN should increase the performance of nanotube-based devices near room temperature. We note that, although it would have been preferable to use known-chirality nanotubes for both tests, the model shows weak dependence of SPP scattering on chirality (supporting information).

In summary, we have measured the temperature-dependent resistivity of a known-chirality metallic SWNT over a wide temperature range, in UHV. Our measurements eliminate adsorbates, acoustic and optical phonons as the cause for the anomalously low $L_m$ measured for SWNTs and identify the SPP modes as the dominant scatterers. The experiments on SWNT deposited over AlN surface are consistent with this conclusion. The accompanying theoretical analysis that includes the intrinsic and SPP phonon modes reproduces the experiments very well. These results point towards the importance of substrate selection in maximizing the electronic mean free path in SWNT.

Acknowledgements: We acknowledge support from the National Science Foundation under collaborative awards DMR-1006230 (MI) and DMR-1006533 (JH), Honda Motor Co., and Intel Co. BC was funded by an Intel PhD Fellowship.

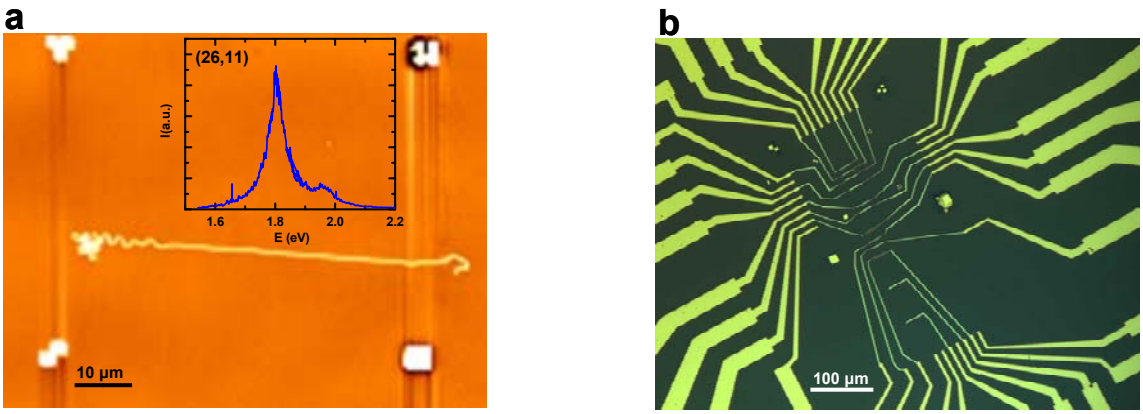


FIG. 1. Chirality-identified SWNT device fabrication
a) AFM image of (26, 11) SWNT transfer printed over 300 nm silicon oxide between gold alignment marks. Rayleigh scattering spectrum of the transferred SWNT (inset). b) Optical microscope image of electrode pattern over SWNT. The inner electrodes are Pd while the outer contacting pads are Ti/Au.

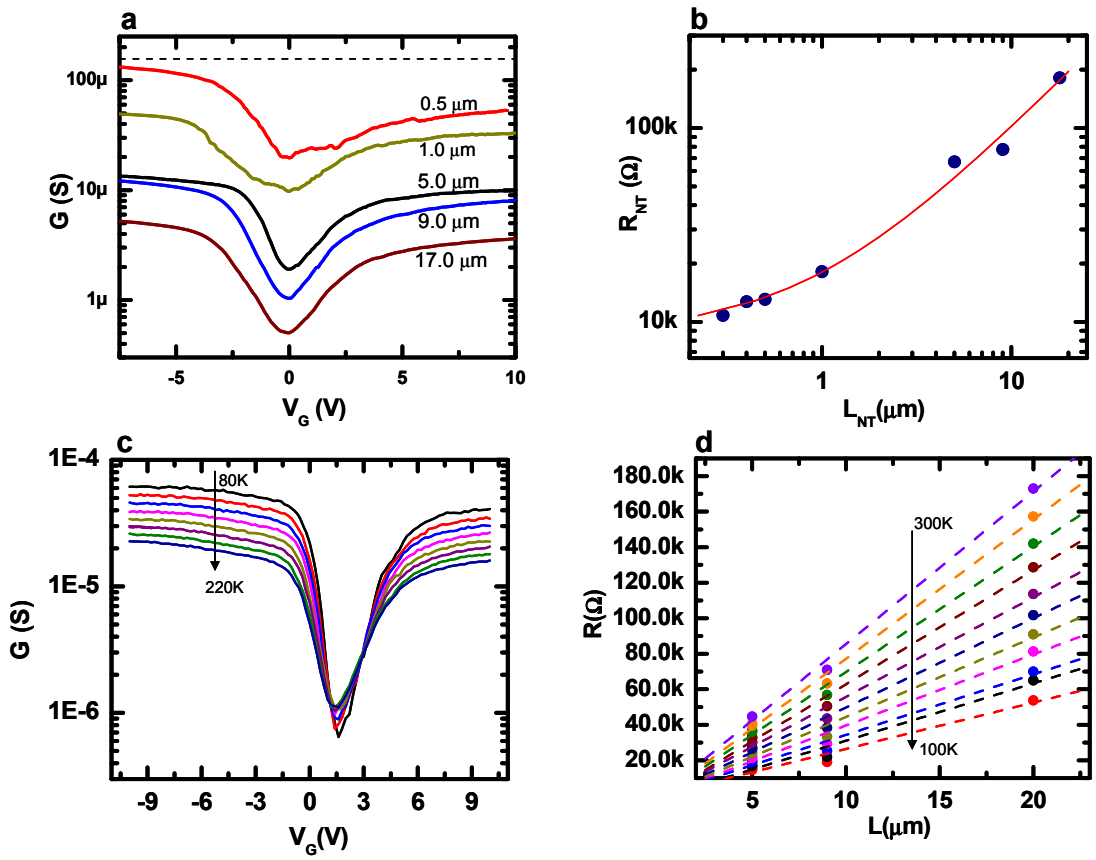


FIG. 2. SWNT resistance measurements at varying channel lengths
a) G vs. $V_g$ for the (26, 11) SWNT (T=300K). Dashed line corresponds to $G=4e^2/h$, conductance of a 4-fold degenerate sublevel b) Log-log plot for R vs. *L* at T=300K. Solid line is fit to the data. c) G vs. $V_g$ for a 7 µm SWNT section, at 20K intervals d) R vs. *L* at varying T.

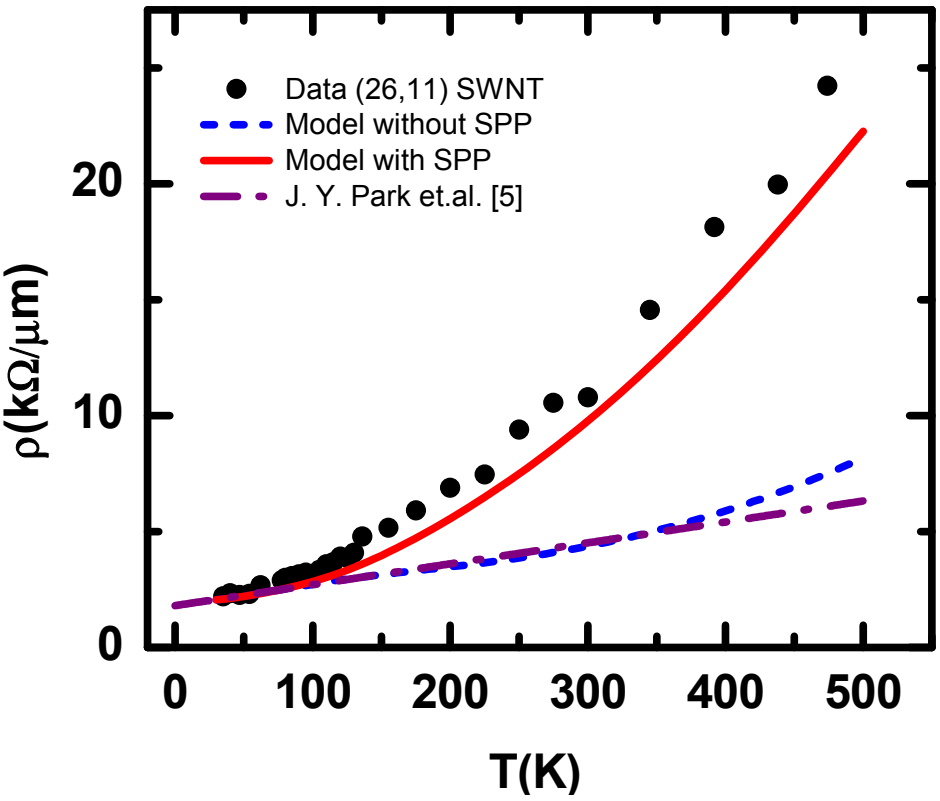


FIG. 3. Resistivity vs. Temperature for (26,11) SWNT.
The dot-dash line represents the calculated resistivity originating from nanotube acoustic phonons using electron scattering rates from ref[5]. Small dash lines show simulation without including SPP scattering. Solid line show model results with SPP scattering.

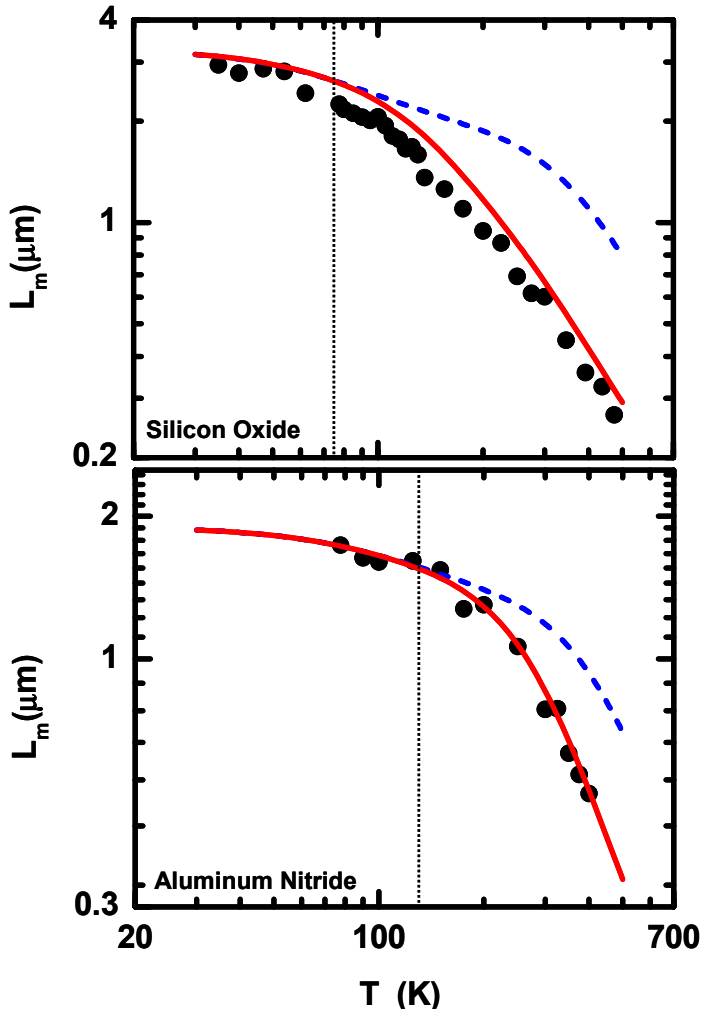


FIG. 4. SWNT mean free path vs. temperature on $SiO_2$ and AlN surfaces

a) $L_m$ vs. T for (26, 11) SWNT on $SiO_2$ b) $L_m$ vs. T for a (17, 15) semiconducting SWNT with d~2.2 nm on ALN. In both plots, the dashed lines represents simulation results using nanotube phonons only, while the solid lines represents results with SPP phonons included. Vertical dotted lines represent the temperature where tube phonon calculations diverge from SPP calculations.

1. S. List et al., Microelectronic Engineering **83**,2200 (2006).
2. R. H. Baughman, A. A. Zakhidov and W. A. de Heer, Science **297**,787 (2002).
3. A. Javey et al., Physical Review Letters **92**,106804 (2004).
4. M. S. Purewal et al., Physical Review Letters **98**,186808 (2007).
5. J. Y. Park et al., Nano Lett. **4**,517 (2004).
6. D. Mann et al., Nano Letters **3**,1541 (2003).
7. H. Suzuura and T. Ando, Physical Review B **65**,235412 (2002).
8. C. L. Kane et al., Europhys. Lett **41**,683 (1998).
9. P. Sundqvist et al., Nano Lett. **7**,2568 (2007).
10. V. Perebeinos, J. Tersoff and P. Avouris, Physical Review Letters **94**,086802 (2005).
11. G. Pennington and N. Goldsman, Physical Review B **68**,045426 (2003).
12. Z. Yao, C. L. Kane and C. Dekker, Physical Review Letters **84**,2941 (2000).
13. L. M. Huang et al., J. Phys. Chem. B **108**,16451 (2004).
14. B. Chandra et al., Physica Status Solidi B-Basic Solid State Physics **243**,3359 (2006).
15. M. Y. Sfeir et al., Science **312**,554 (2006).
16. M. Y. Sfeir et al., Science **306**,1540 (2004).
17. X. M. H. Huang et al., Nano Letters **5**,1515 (2005).
18. M. Ouyang et al., Science **292**,702 (2001).
19. V. V. Deshpande et al., Science **323**,106 (2009).
20. S. Heinze et al., Physical Review Letters **89,** 106801 (2002).
21. E. Pop et al., Journal of Applied Physics **101**,093710 (2007).
22. V. Perebeinos and J. Tersoff, Physical Review B **79**,241409 (2009).
23. J. H. Chen et al., Nature Nanotechnology **3**,206 (2008).
24. V. Perebeinos et al., Nano Letters **9**,312 (2009).
25. S. Q. Wang and G. D. Mahan, Physical Review B **6**,4517 (1972).
26. A. G. Petrov and S. V. Rotkin, Physical Review B **70**, 035408 (2004).
27. M. V. Fischetti, D. A. Neumayer and E. A. Cartier, Journal of Applied Physics **90**,4587 (2001).